*International Journal of Minerals, Metallurgy and Materials*
*Volume 29, Number 10, October 2022, Page 1862*
**https://doi.org/10.1007/s12613-021-2385-0**

# Phosphorus reduction behavior of high-phosphate iron ore during hydrogen-rich sintering

*Yanbiao Chen*, *Wenguo Liu*, *and Haibin Zuo*✉

State Key Laboratory of Advanced Metallurgy, University of Science and Technology Beijing, Beijing 100083, China
(Received: 31 July 2021; revised: 22 November 2021; accepted: 23 November 2021)

**Abstract:** High-phosphorus iron ore resource is considered a refractory iron ore because of its high-phosphorus content and complex ore phase structure. Therefore, the development of innovative technology to realize the efficient utilization of high-phosphorus iron ore resources is of theoretical and practical significance. Thus, a method for phosphorus removal by gasification in the hydrogen-rich sintering process was proposed. In this study, the reduction mechanism of phosphorus in hydrogen-rich sintering, as well as the reduction kinetics of apatite based on the non-isothermal kinetic method, was investigated. Results showed that, by increasing the reduction time from 20 to 60 min, the dephosphorization rate increased from 10.93% to 29.51%. With apatite reduction, the metal iron accumulates, and part of the reduced phosphorus gas is absorbed by the metal iron to form stable iron–phosphorus compounds, resulting in a significant reduction of the dephosphorization rate. Apatite reduction is mainly concentrated in the sintering and burning zones, and the reduced phosphorus gas moves downward along with flue gas under suction pressure and is condensed and adsorbed partly by the sintering bed when passing through the drying zone and over the wet zone. As a result, the dephosphorization rate is considerably reduced. Based on the Ozawa formula of the iso-conversion rate, the activation energy of apatite reduction is 80.42 kJ/mol. The mechanism function of apatite reduction is determined by a differential method (i.e., the Freeman–Carroll method) and an integral method (i.e., the Coats–Redfern method). The differential form of the equation is $f(\alpha) = 2(1-\alpha)^{1/2}$, and the integral form of the equation is $G(\alpha) = 1-(1-\alpha)^{1/2}$.

**Keywords:** hydrogen-rich sintering; dephosphorization; reduction mechanism; kinetics; thermogravimetry

## 1. Introduction

With the continuous expansion of the scale of China's iron and steel industry, iron ore consumption has been increasing year by year; meanwhile, the high dependence on imported iron ore and the fluctuating prices have seriously affected the stable development of China's iron and steel industry [1–3]. Therefore, focusing on the development and utilization of domestic complex refractory iron ore and increasing the self-sufficiency rate of iron ore have strategic significance for ensuring the sustainable and stable development of the iron and steel industry. China is rich in high-phosphate iron ore resources; however, it has not been fully utilized because of its low grade, high-phosphorus content, complex mineral structure, fine grain size, and close symbiotic relationship between minerals [4–5].

The efficient utilization of high-phosphate iron ore has become one of the main topics for researchers, and a large number of experiments have been conducted. At present, the main methods used to treat high-phosphate iron ore include beneficiation, reduction melting, chemical, and bioleaching methods. The main advantage of the beneficiation method is its low cost; however, the dephosphorization efficiency is poor when using a single beneficiation method. Although the comprehensive beneficiation method can obtain relatively higher dephosphorization efficiency, the high-energy consumption and large-scale equipment make it impossible to realize large-scale industrial popularization [6–8]. The dephosphorization rate of the reduction–melting method is high; however, the high equipment requirements and costs make it impossible to realize industrial production [9–10]. The chemical method is simple, and dephosphorization can be achieved by immersing the high-phosphate iron ore in the leaching solution, which has an obvious effect and low iron loss. However, the use of a large number of chemical leaching agents causes environmental pollution, and the low productivity limits its popularization [11–13]. Bioleaching dephosphorization mainly depends on microbial metabolism to produce acid to dissolve phosphorus minerals; however, the metabolic acid reacts with the magnesium and calcium ions. The mineral dissolution method has the advantages of low cost and less environmental pollution; however, it is still in the experimental research stage because of its long production cycle [14–15]. In summary, conducting relevant basic research on innovative dephosphorization technology to realize the efficient development and utilization of high-phos-

✉ Corresponding author: Haibin Zuo E-mail: zuohaibin@ustb.edu.cn

phorus iron ore is of theoretical and practical significance.

In recent years, in the face of global climate change, reducing $CO_2$ emissions and implementing low-carbon production have become urgent tasks for the iron and steel industry [16–18]. Sintering production accounts for approximately 15% of the total carbon emissions from blast furnace (BF) and basic oxygen furnace processes. To reduce carbon emissions, JFE Steel Corporation has developed an innovative sintering process aided by the injection of hydrogen-rich gas fuel [19]. Hydrogen-rich sintering provides a strong reducing atmosphere, prolongs the high-temperature section, and improves the sintering porosity and sintering suction operation; therefore, it is fit for the reduction and removal operations of some specific elements, such as phosphorus removal from the iron ore containing apatite [20–22]. The reduced phosphorus is volatilized into the flue gas and discharged, finally realizing the gasification and removal of phosphorus via hydrogen-rich sintering. The dephosphorized sinter can be used as the BF burden, and the phosphorus gas recovered from flue gas can be used in many fields, such as the pesticide and chemical industries [23–24]. Researchers have conducted numerous experiments on phosphorus removal in the sintering process of high-phosphorus iron ore. Zhang *et al.* [25] investigated the effect of different process conditions on sintering gasification dephosphorization through micro-sintering experiments. Their results showed that the optimal dephosphorization rate was conducted with a 4wt% carbon mixing ratio, 1.41wt% $SiO_2$, and 1.36wt% $CaCl_2$, as well as controlled basicity of 1.2. The corresponding dephosphorization rate was 18.30%. Zhang *et al.* [25] also conducted exploratory experiments on mini pellet and microwave sintering dephosphorization processes. Their results showed that the microwave sintering dephosphorization process could achieve the optimal dephosphorization rate when adding 5wt% carbon, 0.75wt% $SiO_2$, and 1.5wt% $CaCl_2$, with controlled basicity of 1.4. The corresponding dephosphorization rate was 25.71%. The sintering atmosphere is the oxidizing atmosphere macroscopically, and the reducing atmosphere exists around the carbon particles. Hydrogen-rich sintering provides a strong reducing atmosphere, prolongs the high-temperature section, and improves the sintering porosity; therefore, it is fit for phosphorus removal from the iron ore containing apatite.

This study aims to analyze the reduction behavior and the reduction and gasification kinetics of apatite during hydrogen-rich sintering. In this experiment, pure substances were used to simulate the chemical composition of high-phosphorus iron ore, which was roasted in a reduction furnace in the form of tablet pressing. The phase transformation and distribution of phosphorus under different reduction times were analyzed by X-ray diffraction (XRD) and scanning electron microscopy–energy-dispersive X-ray spectroscopy (SEM–EDS). The mechanism of reduction dephosphorization of high-phosphorus iron ore during sintering was explored. The non-isothermal reduction kinetics of apatite at different heating rates in a hydrogen-rich atmosphere was investigated by a thermogravimetric analyzer. Moreover, the reaction mechanism function was determined by the linear fitting of different kinetic models.

## 2. Experimental

### 2.1. Reduction experiments

The experiment on hydrogen-rich sintering reduction of high-phosphate iron ore was conducted in a programmed reduction furnace, as shown in Fig. 1(b). The experimental process included mixing, tablet pressing, and reduction roasting. In the experiment, an analytical reagent was used to simulate the chemical composition of high-phosphate iron ore, and the mass ratio of the experimental mixture is shown in Table 1. The content of calcium phosphate was increased in the mixture to observe the reduction process of apatite more clearly. To reduce the influence of impurities, graphite was selected instead of coke as the reducing agent. The thermodynamic calculation results showed that the addition of $Na_2CO_3$ could promote apatite reduction; thus, 1wt% $Na_2CO_3$ was added in the experiment [26]. The 5 g mixture was pressed under a constant pressure of 5 MPa to form a cylindrical sample with a diameter of 20 mm. The cylindrical sample was dried at 105°C for 2 h. The preliminary experimental results showed that, in the hydrogen-rich atmosphere, when the reduction temperature is 1100°C, the dephosphorization rate reaches its peak. Therefore, the pressed tablets were heated from room temperature to 1100°C at a rate of 10°C/min in a reduction furnace. Then, reduction experiments were conducted at intervals of 10 min within 60 min. During the reduction process, the flow rates of $H_2$ and $N_2$ were 2 and 5 L/min, respectively. After the reduction experiments, the sample was cooled to room temperature with the furnace under $N_2$ protection. The phosphorus content was determined by chemical analysis. The phase composition was determined by XRD (RIGAKU, D/Max 2500, Japan) with a Cu target, with a scanning angle ranging from 10° to 90° and a step size of 0.02°. The microstructure and element distribution of the sample were observed by SEM–EDS (Regulus8100, Japan).

The multipoint sampling before and after roasting was used to detect the phosphorus content, and the dephosphorization rate was calculated according to the following formula:

$$\eta = \left(1 - \frac{P_1 \times M_1}{P_0 \times M_0}\right) \times 100\% \quad (1)$$

where $\eta$ is the dephosphorization rate; $P_0$ and $P_1$ are the phosphorus contents in the tablet before and after reduction, respectively; and $M_0$ and $M_1$ are the mass of the tablets before and after reduction, respectively.

### 2.2. Thermogravimetric measurement and thermal analysis kinetics

The reduction kinetics of apatite was investigated using temperature-programmed thermogravimetry. The experimental device is shown in Fig. 1(c). To exclude the interference affecting the reduction kinetics of apatite during hydrogen-rich sintering, iron oxides were removed from the experimental process. The mass ratio of the experimental mixture

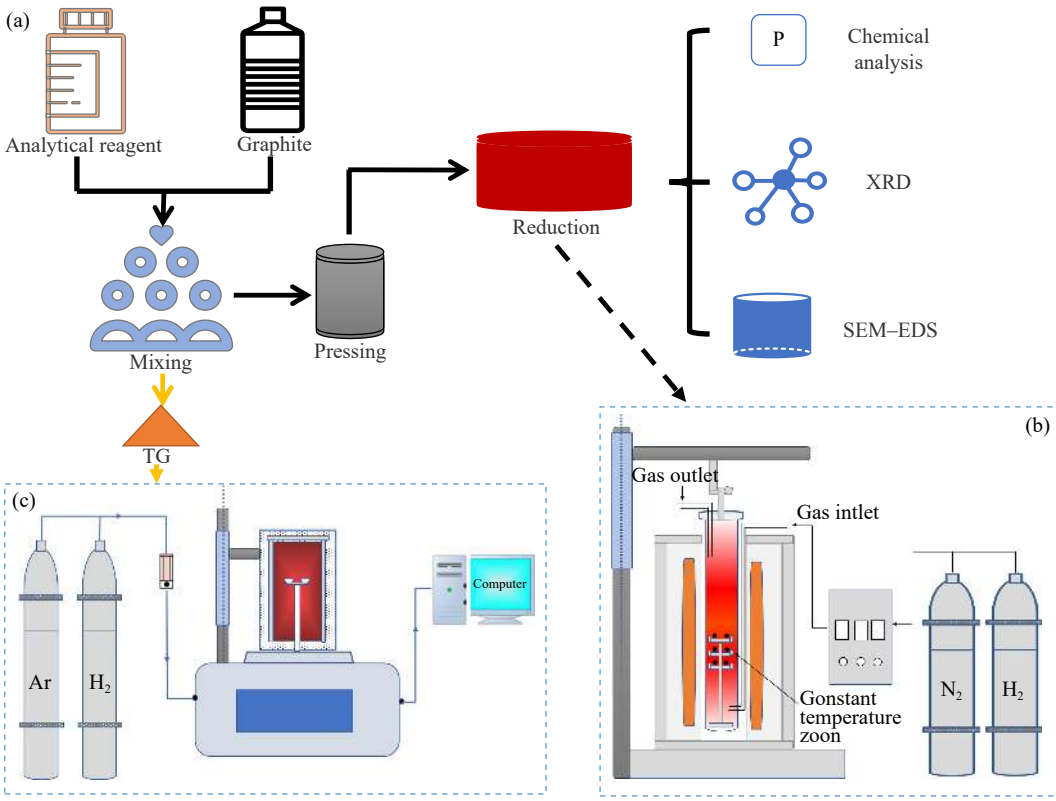


**Fig. 1. (a) Flow diagram of the reduction experiments; (b) schematic of the programmed reduction furnace; (c) schematic of the thermogravimetric analysis system.**

is shown in Table 2. Approximately 10 mg of the mixed sample was placed in a cylindrical crucible and linearly heated to a certain temperature (i.e., 1400°C). The heating rate was controlled at 5, 10, and 15°C/min. The gas flow was controlled by a mass flowmeter at 100 and 80 mL/min for argon and hydrogen, respectively.

**Table 1. Mass ratio of the mixture in the reduction experiment**

| Composition | Content of raw ore / wt% | Simulation mass ratio |
|---|---|---|
| $Fe_2O_3$ | 57.40 | 58 |
| CaO | 5.10 | 5 |
| $SiO_2$ | 10.97 | 11 |
| $Ca_3(PO_4)_2$ | 7.53 | 11 |
| MgO | 1.97 | 2 |
| $Al_2O_3$ | 1.00 | 1 |
| C | — | 5 |
| $Na_2CO_3$ | — | 1 |

**Table 2. Mass ratio of the mixture in the thermogravimetric experiment**

| Composition | Content of raw ore / wt% | Simulation mass ratio |
|---|---|---|
| $Fe_2O_3$ | 57.40 | 0 |
| CaO | 5.10 | 5 |
| $SiO_2$ | 10.97 | 11 |
| $Ca_3(PO_4)_2$ | 7.53 | 11 |
| MgO | 1.97 | 2 |
| $Al_2O_3$ | 1.00 | 1 |
| C | — | 5 |
| $Na_2CO_3$ | — | 1 |

## 3. Kinetic analysis of apatite reduction

### 3.1. Kinetic reaction equation

The apatite reduction reaction in the hydrogen-rich sintering process is a gas–solid reaction, and its reaction is shown in Eq. (2):

$$a\mathrm{A(g)} + b\mathrm{B(s)} = g\mathrm{G(g)} + s\mathrm{S(s)} \tag{2}$$

where A(g) and G(g) are gaseous reactants and products, B(s) and S(s) are solid reactants and products.

In the thermogravimetric experiment, the conversion rate $\alpha$ is defined as the ratio of the mass loss at a certain time to the theoretical maximum mass loss [27] and expressed as follows:

$$\alpha = \frac{W_0 - W_t}{W_0 - W_\infty} \tag{3}$$

where $W_0$, $W_t$, and $W_\infty$ are the initial, instantaneous, and final masses of the sample, respectively.

The basic kinetic equation that expresses the reduction rate as a function of temperature is shown in Eq. (4) [28]:

$$\frac{\mathrm{d}\alpha}{\mathrm{d}t} = f(\alpha) \times k(T) \tag{4}$$

where $\mathrm{d}\alpha/\mathrm{d}t$ is the reaction rate, $f(\alpha)$ is the reaction mechanism function, and $k(T)$ is the rate constant.

The relationship between rate constant $k(T)$ and reaction temperature $T$ follows the Arrhenius formula, as shown in Eq. (5):

$$k(T) = A\exp\left(-\frac{E_a}{RT}\right) \quad (5)$$

where $A$ is the pre-exponential factor, $E_a$ is the activation energy, and $R$ is the universal gas constant.

The basic dynamic equation can be further obtained, as shown in Eq. (6):

$$\frac{d\alpha}{dt} = A\exp\left(-\frac{E_a}{RT}\right)f(\alpha) \quad (6)$$

In the non-isothermal thermogravimetric experiment, the reaction is conducted at a programmed heating rate, and the heating rate $\beta$ is expressed as Eq. (7). Eq. (6) is further transformed into Eq. (8):

$$\beta = \frac{dT}{dt} \quad (7)$$

$$\frac{d\alpha}{dT} = \frac{A}{\beta}\exp\left(-\frac{E_a}{RT}\right)f(\alpha) \quad (8)$$

### 3.2. Thermal analysis kinetics

The non-isothermal method was used to analyze the reduction and gasification kinetics of apatite during hydrogen-rich sintering. An integral method (i.e., Ozawa method) [29] was employed to deal with the experimental data to obtain the activation energy, as shown in Eq. (9):

$$\lg\beta = \lg\left[\frac{AE_a}{RG(\alpha)}\right] - 2.315 - 0.4567\frac{E_a}{RT} \quad (9)$$

where $G(\alpha)$ is the integral form of the mechanism function $f(\alpha)$, defined as $G(\alpha) = \int_0^\alpha \frac{d\alpha}{f(\alpha)}$. Under the condition of a certain conversion rate $\alpha$, the temperature $T$ corresponding to different temperature increase rates $\beta$ is obtained. According to the principle of the least square method, $\lg\beta$ is linearly regressed to $1/T$, and the activation energy $E_a$ can be further calculated from the slope of the fitting line.

### 3.3. Solution of the reaction mechanism function

At present, the reaction mechanism function of the reduction and gasification kinetics of apatite in the hydrogen-rich sintering process has not been reported; thus, the reaction mechanism function needs to be preliminarily explored. Bagchi and Sen [30–31] proposed the combination of the differential and integral methods to treat the non-isothermal kinetic data to confirm the reaction mechanism function. The commonly used kinetic treatment methods (non-isothermal) are the Freeman–Carroll method (differential method) and the Coats–Redfern method (integration method), as shown in Eqs. (10) and (11):

$$\ln\left[\frac{d\alpha/dt}{f(\alpha)}\right] = \ln A - \frac{E_a}{RT} \quad (10)$$

$$\ln\left[\frac{G(\alpha)}{T^2}\right] = \ln\frac{AR}{\beta E_a} - \frac{E_a}{RT} \quad (11)$$

Through the linear fitting of different kinetic models, the linear correlation coefficient ($N$) of each model was obtained, by which the mechanism function was determined. Table 3 shows the integral and differential forms of the mathematical models of the chemical reaction [18,32].

**Table 3. Common mathematical models of the chemical reaction [18,32]**

| Model | Symbol | $G(\alpha)$ | $f(\alpha)$ | Mechanism |
|---|---|---|---|---|
| Reaction-order models | F1 | $-\ln(1-\alpha)$ | $1-\alpha$ | First order |
| | F1.5 | $2[(1-\alpha)^{-1/2}-1]$ | $(1-\alpha)^{3/2}$ | 1.5 order |
| | F2 | $(1-\alpha)^{-1}-1$ | $(1-\alpha)^2$ | Second order |
| | F3 | $1/2[(1-\alpha)^{-1}-1]$ | $(1-\alpha)^3$ | Third order |
| Diffusion models | D1 | $\alpha^2$ | $1/(2\alpha)$ | 1D Parabolic |
| | D2 | $(1-\alpha)\ln(1-\alpha)+\alpha$ | $-\ln(1-\alpha)^{-1}$ | 2D Valensi |
| | D3 | $[1-(1-\alpha)^{1/3}]^2$ | $1.5(1-\alpha)^{2/3}[1-(1-\alpha)^{1/3}]^{-1}$ | 3D Jander |
| Phase-boundary-controlled models | R1 | $\alpha$ | 1 | Infinite slab |
| | R2 | $1-(1-\alpha)^{1/2}$ | $2(1-\alpha)^{1/2}$ | Contracting cylinder |
| | R3 | $1-(1-\alpha)^{1/3}$ | $3(1-\alpha)^{2/3}$ | Contracting sphere |
| Nucleation models | A1 | $-\ln(1-\alpha)$ | $1-\alpha$ | Aevrami–Erofeev, $m=1$ |
| | A2 | $[-\ln(1-\alpha)]^{1/2}$ | $2(1-\alpha)[-\ln(1-\alpha)]^{1/2}$ | Aevrami–Erofeev, $m=1$ |
| | A3 | $[-\ln(1-\alpha)]^{1/3}$ | $3(1-\alpha)[-\ln(1-\alpha)]^{2/3}$ | Aevrami–Erofeev, $m=1$ |

## 4. Results and discussion

### 4.1. Reduction process and conversion at different heating rates

Fig. 2 shows the mass loss curves of apatite reduction at different heating rates (i.e., 5, 10, and 15°C/min). Notably, the reduction mass loss law of apatite was the same at different heating rates, and the thermogravimetric curve shifted regularly to the high-temperature region with the increase in the heating rate. The higher the heating rate was, the more serious the temperature lag phenomenon and the higher the measured value of the end temperature of mass loss. According to the shape of the curve, the reduction process could be divided into the initial, intermediate, and final stages. In the initial stage, the degree of reduction increased at a slow rate. In the intermediate stage, the degree of reduction increased rapidly. In the final stage, a deceleration trend occurred. With the increase in the heating rate, the degree of reduction of the

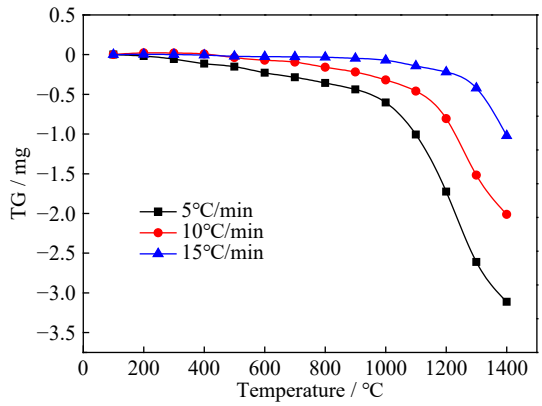


**Fig. 2. Mass loss curves of apatite reduction at different heating rates.**

same reduction stage decreased. With the decrease in the heating rate, the reduction time and effective reaction increased, which provided more chemically active sites for the reaction of apatite with the reducing agent.

The evolution of the conversion curves with the temperature at different heating rates is shown in Fig. 3. Improving the heating rate made the conversion curve shift to the high-temperature region, which means that a higher heating rate could only lead to a lower conversion at the same temperature. Notably, the conversion rate increased slowly when the temperature was lower than 1000°C. After the reaction was accelerated, the mass loss increased, indicating that a large amount of phosphorus was discharged continuously. The results showed that the increase in the reduction temperature is beneficial to the reduction reaction. Theoretically, the higher the reduction temperature is, the higher the dephosphorization rate. However, a high reduction temperature improves the kinetic conditions of phosphorus gas migrating to metallic iron, and the trend of the mass loss curve slows down. According to the change of the mass loss curve at different temperatures, the dephosphorization reaction mainly occurs in the sintering and combustion zones at high temperatures.

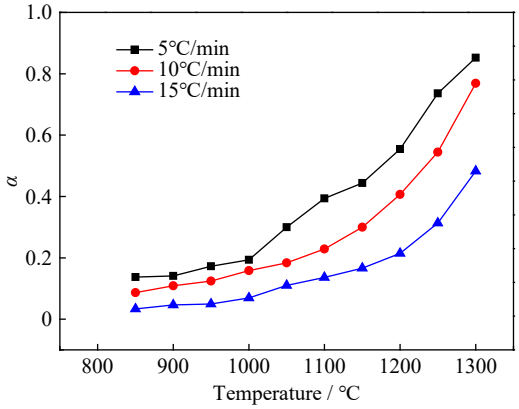


**Fig. 3. Conversion curves of apatite reduction at different heating rates.**

### 4.2. Activation energy of the reaction and reaction mechanism

The reaction temperature of the same conversion at different heating rates is shown in Table 4. According to the principle of the least square method, the scatter points were linearly fitted into a straight line, and the activation energy of the reaction could be calculated according to the slope. Taking the conversion rate of 0.4 as an example, the conversion results of corresponding data are shown in Table 5. According to the principle of the least square method, lg $\beta$ is linearly regressed to $1/T$, as shown in Fig. 4. The fitted slope of the straight line was substituted into the expression $0.4567E_a/R$, and the activation energy of the reaction at this conversion rate was 107.84 kJ/mol. The activation energy of each conversion rate is shown in Table 6. Based on the Ozawa formula of the iso-conversion rate, the activation energy of apatite reduction during hydrogen-rich sintering was 80.42 kJ/mol.

The commonly used kinetic mechanism functions (Table 3) were selected to analyze the reduction data.

**Table 4. Reaction temperature of the same conversion at different heating rates** °C

| $\alpha$ | $\beta$ / (°C·min$^{-1}$) | | |
|---|---|---|---|
| | 5 | 10 | 15 |
| 0.1 | 766.40 | 898.93 | 1029.38 |
| 0.2 | 988.09 | 1085.84 | 1167.50 |
| 0.3 | 1049.60 | 1153.28 | 1241.54 |
| 0.4 | 1103.78 | 1201.19 | 1274.02 |

**Table 5. Values of $T^{-1}$ and lg $\beta$ when the conversion rate is 0.4**

| Heating rate / (°C·min$^{-1}$) | $t$ / °C | $T$ / K | $T^{-1}$ / (10$^{-3}$ K$^{-1}$) | lg[$\beta$ / (°C·min$^{-1}$)] |
|---|---|---|---|---|
| 5 | 1103.78 | 1376.93 | 0.72625 | 0.70 |
| 10 | 1201.19 | 1474.34 | 0.67826 | 1.00 |
| 15 | 1274.02 | 1547.17 | 0.64634 | 1.17 |

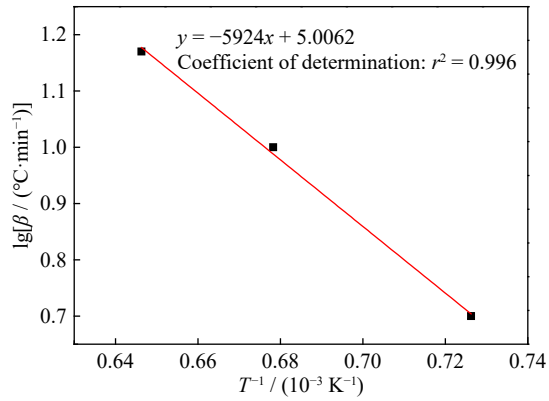


**Fig. 4. Linear fitting results of $T^{-1}$ and lg $\beta$.**

**Table 6. Activation energy of the reaction under different conversion rates**

| Conversion rate | Activation energy / (kJ·mol$^{-1}$) | Average / (kJ·mol$^{-1}$) |
|---|---|---|
| 0.1 | 44.43 | 82.42 |
| 0.2 | 87.35 | |
| 0.3 | 90.07 | |
| 0.4 | 107.84 | |

Through the linear fitting of different kinetic models, the apparent activation energy ($E_a$) and the correlation coefficient ($N$) were calculated and compared to determine which model would be a suitable match for the experimental data conversion. As shown in Table 7, among the apparent activation energies of different reaction models calculated by the Freeman–Carroll method, the apparent activation energies of 90.97, 101.59, and 68.83 kJ/mol were close to 82.42 kJ/mol. The corresponding mechanism functions are R2, R3, and A2, and the correlation coefficients are 0.99274, 0.99602, and 0.99728, respectively. Among the apparent activation energies of different reaction models calculated by the Coats–Redfern method, the apparent activation energies of 83.99, 84.95, and 82.90 kJ/mol are close to 82.42 kJ/mol. The corresponding mechanism functions are F1, R2, and A1, and the correlation coefficients are 0.95427, 0.95629, and 0.95427, respectively. The results of the two calculation methods intersect, and the most likely mechanism function is R2, a contracting cylinder. The differential form of the equation is $f(\alpha) = 2(1-\alpha)^{1/2}$, and the integral form of the equation is $G(\alpha) = 1-(1-\alpha)^{1/2}$.

**Table 7. Kinetic parameters of different chemical reaction models**

| Mechanism symbol | Freeman–Carroll | | Coats–Redfern | |
|---|---|---|---|---|
| | $N$ | $E_a$ / (kJ·mol$^{-1}$) | $N$ | $E_a$ / (kJ·mol$^{-1}$) |
| F1 | 0.99102 | 122.83 | 0.95427 | 83.99 |
| F1.5 | 0.97488 | 154.70 | 0.94487 | 10.18 |
| F2 | 0.95857 | 186.56 | 0.93159 | 120.56 |
| F3 | 0.93279 | 250.29 | 0.93159 | 120.56 |
| D1 | 0.96705 | 139.06 | 0.96322 | 136.80 |
| D2 | 0.98550 | 167.13 | 0.96718 | 153.14 |
| D3 | 0.98550 | 199.42 | 0.96723 | 172.54 |
| R1 | 0.89865 | 59.11 | 0.95427 | 75.93 |
| R2 | 0.99274 | 90.97 | 0.95629 | 84.95 |
| R3 | 0.99602 | 101.59 | 0.95669 | 94.71 |
| A1 | 0.99102 | 122.84 | 0.95427 | 82.90 |
| A2 | 0.99728 | 68.83 | 0.91738 | 30.89 |
| A3 | 0.99600 | 50.82 | 0.80143 | 12.89 |

### 4.3. Dephosphorization rate and phase transition during roasting

In the reduction process, part of apatite is reduced and volatilized in the form of gas, and the phosphorus content of the sample before and after the reaction is determined to calculate the dephosphorization rate. Fig. 5 shows the evolution of the dephosphorization rate along with roasting time at 1100°C. The dephosphorization rate increased from 10.93% to 29.51%, with the reduction time increasing from 20 to 60 min during hydrogen-rich sintering. According to the kinetic principle, with the increase in the reduction time, the effect of the limiting element on the apatite reduction reaction was reduced. Thus, the reaction was fully completed and the dephosphorization rate was improved. Prolonging the high-temperature section of the hydrogen-rich sintering bed can effectively improve the thermodynamic and kinetic conditions of reduction dephosphorization, which is beneficial to apatite reduction. However, the increase in the reduction time will decrease the production efficiency.

The phase of the reduced sample was analyzed by XRD. The results are shown in Fig. 6. Iron oxides were reduced to metallic iron step by step in the order of $Fe_2O_3 \rightarrow Fe_3O_4 \rightarrow FeO \rightarrow Fe$. When the reduction time was 20 min, the diffraction peaks of Fe, $Fe_3O_4$, and FeO were detected, indicating that iron oxide was not completely reduced at this time. The intermediate product, i.e., solid-state FeO, reacted with $SiO_2$

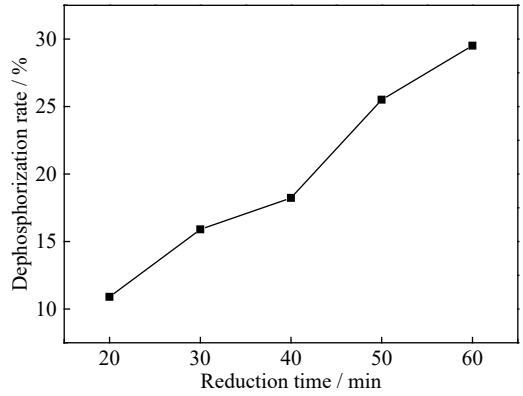


**Fig. 5. Effect of sintering time on the dephosphorization rate of sinter.**

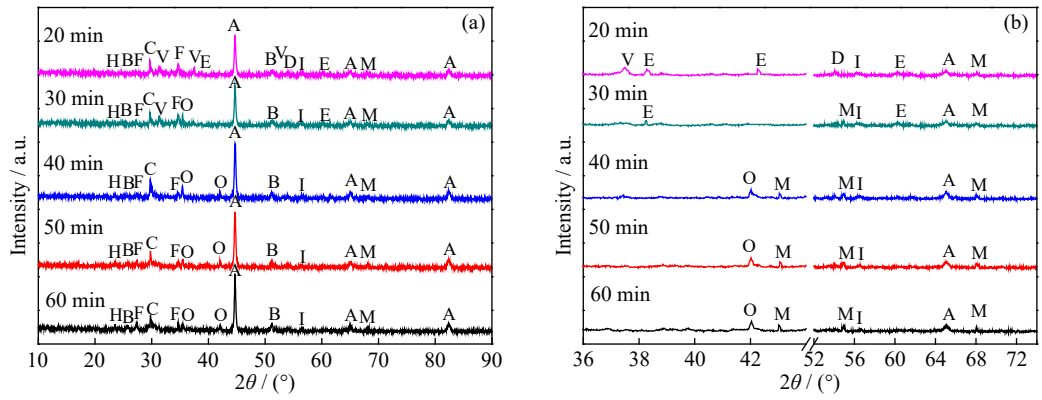


**Fig. 6. (a) Phase composition of the reduced samples from X-ray diffraction analysis and (b) partially enlarged view of the zone with the peaks of E and M (A—Fe, B—$Fe_2SiO_4$, C—$CaSiO_3$, D—$Fe_3O_4$, E—FeO, F—$Na_2CaSi_5O_{12}$, H—$NaAlSiO_4$, I—$FeAl_2O_4$, M—$Fe_3C$, O—$Fe_2P$, and V—$Ca_3(PO_4)_2$).**

and $Al_2O_3$ to form fayalite and spinel. Moreover, the formed metallic iron underwent a carburization reaction to form $Fe_3C$. When the reduction time reached 30 min, the existence of $Fe_2P$ was detected because of the migration of phosphorus to metallic iron. With the increase in the reduction time, apatite was reduced completely and the diffraction peak of apatite disappeared at 40 min.

With the progress of the reaction, $Na_2CO_3$ reacted with CaO, $SiO_2$, and $Al_2O_3$ to form $Na_2CaSi_5O_{12}$ and $NaAlSiO_4$ with low melting points. The increase in the liquid phase content of the system improved the fluidity, and the increase in the contact area improved the mass transfer kinetic conditions between carbon-containing, iron-oxide-containing, and phosphorus-containing minerals, which accelerated the reduction of iron oxide and apatite. During the reduction process, sodium carbonate decomposed into sodium oxide and carbon dioxide, which promoted the gasification of carbon and further boosted the reduction reaction. Moreover, alkali metals could cause the lattice deformation of iron oxide, and the lattice transformation became conducive to the formation of porous iron, which promoted the diffusion capacity of mass in the sintering bed [33].

### 4.4. Distribution characteristics of phosphorus in roasting products

The mineral reaction process in the reduction process was preliminarily explored by XRD detection. However, the change process of apatite was not explained clearly and in detail. Therefore, the SEM–EDS method was used to explain the mineral evolution of high-phosphate iron ore and the process of phosphorus migrating to the iron ore through the analysis of the microscopic mineral change law.

Fig. 7 shows the element distribution of the sample at the reduction times of 20, 40, and 60 min, corresponding to (a), (b), and (c), respectively. When the reduction time was 20 min, phosphorus and calcium exhibited an overlapping distribution, and phosphorus existed mainly in the form of apatite, indicating that a small amount of apatite was reduced and migrated to the iron phase. When the reduction time was 40 min, more phosphorus began to migrate to metallic iron and presented a disordered microstructure. When the reduction time was 60 min, the metal iron increased gradually and accumulated, and phosphorus in the metal iron was uniformly distributed. The main reason was that iron oxide was mainly reduced at the initial stage of reduction, and at that time, the carbon content in iron was low. With the mineral reaction process, the carburization of iron led to the increase in liquid iron, providing the appropriate conditions for the migration of phosphorus to metallic iron. With apatite reduction, the reduced phosphorus extended gradually from the edge to the interior of the iron phase, resulting in the increase in the phosphorus content in the iron phase.

### 4.5. Reduction mechanism of the hydrogen-rich sintering process of high-phosphate iron ore

The reduction mechanism of the hydrogen-rich sintering process of high-phosphate iron ore is shown in Fig. 8. Under the reducing atmospheres of carbon and hydrogen, iron oxide was reduced systematically. Then, the metal phase aggregated and grew during the mineral reaction process. Finally, only the metal and slag phases with uniform texture existed in the sinter, and the boundary between them was obvious. The reduction equations are expressed as Eqs. (12) to (17).

$$3Fe_2O_3 + H_2 = 2Fe_3O_4 + H_2O,\ \Delta_rG_m^{\ominus} = -15547 - 74.4T \quad (12)$$

$$Fe_3O_4 + H_2 = 3FeO + H_2O,\ \Delta_rG_m^{\ominus} = 71940 - 73.62T \quad (13)$$

$$FeO + H_2 = Fe + H_2O,\ \Delta_rG_m^{\ominus} = 23430 - 16.16T \quad (14)$$

$$3Fe_2O_3 + C = 2Fe_3O_4 + CO,\ \Delta_rG_m^{\ominus} = 136893 - 232.16T \quad (15)$$

$$Fe_3O_4 + C = 3FeO + CO,\ \Delta_rG_m^{\ominus} = 200066 - 205.16T \quad (16)$$

$$FeO + C = Fe + CO,\ \Delta_rG_m^{\ominus} = 149289 - 149.12T \quad (17)$$

The reduction of FeO was the most difficult during the entire process. The intermediate product FeO reacted with $SiO_2$ and $Al_2O_3$ in the ore to form iron olivine and spinel, which inhibited the combination of iron and phosphorus to a certain extent. The reaction equations are expressed as Eqs. (18) and (19). At the same time, $Fe_3C$ was formed because of the carburization reaction of metallic iron.

$$2FeO + SiO_2 = Fe_2SiO_4,\ \Delta_rG_m^{\ominus} = 4532 - 25.35T \quad (18)$$

$$FeO + Al_2O_3 = FeAl_2O_4,\ \Delta_rG_m^{\ominus} = -15676 - 0.46T \quad (19)$$

$$3Fe + C = Fe_3C,\ \Delta_rG_m^{\ominus} = 26694 - 24.77T \quad (20)$$

Under the reducing atmospheres of carbon and hydrogen, apatite was reduced to $P_2$ gas with the progress of the reaction, as shown in Eqs. (22) to (27).

$$Na_2CO_3 + Al_2O_3 + 2SiO_2 = 2NaAlSiO_4 + CO_2,\ \Delta_rG_m^{\ominus} = 1469.8 - 177.18T \quad (21)$$

$$Ca_3(PO_4)_2 + 5H_2 + 3Na_2CO_3 + 15SiO_2 = 3Na_2CaSi_5O_{12} + 5H_2O + P_2 + 3CO_2,\ \Delta_rG_m^{\ominus} = -1093.7T + 10^6 \quad (22)$$

$$Ca_3(PO_4)_2 + 5H_2 + 6Na_2CO_3 + 9SiO_2 = 3Na_4CaSi_3O_9 + 5H_2O + P_2 + 6CO_2,\ \Delta_rG_m^{\ominus} = -1357.9T + 1115177 \quad (23)$$

$$Ca_3(PO_4)_2 + 6C + 6SiO_2 + Na_2CO_3 = Na_2Ca_3Si_6O_{16} + P_2 + 7CO,\ \Delta_rG_m^{\ominus} = 1353501 - 1384T \quad (24)$$

$$Ca_3(PO_4)_2 + 11C + 9SiO_2 + 6Na_2CO_3 = 3Na_4Ca_3Si_3O_9 + P_2 + 17CO,\ \Delta_rG_m^{\ominus} = 2331409 - 3127T \quad (25)$$

$$Ca_3(PO_4)_2 + 13C + 9SiO_2 + 3Na_2CO_3 = 3Na_2Ca_2Si_3O_9 + 2P_2 + 16CO,\ \Delta_rG_m^{\ominus} = 2755910 - 2939T \quad (26)$$

$$Ca_3(PO_4)_2 + 8C + 15SiO_2 + 3Na_2CO_3 = 3Na_2CaSi_5O_{12} + P_2 + 11CO,\ \Delta_rG_m^{\ominus} = 1865723 - 2321T \quad (27)$$

The addition of $SiO_2$ and $Na_2CO_3$ significantly decreased the reduction temperature of apatite and sufficiently reduced apatite [26]. The formation of a low-melting-point slag

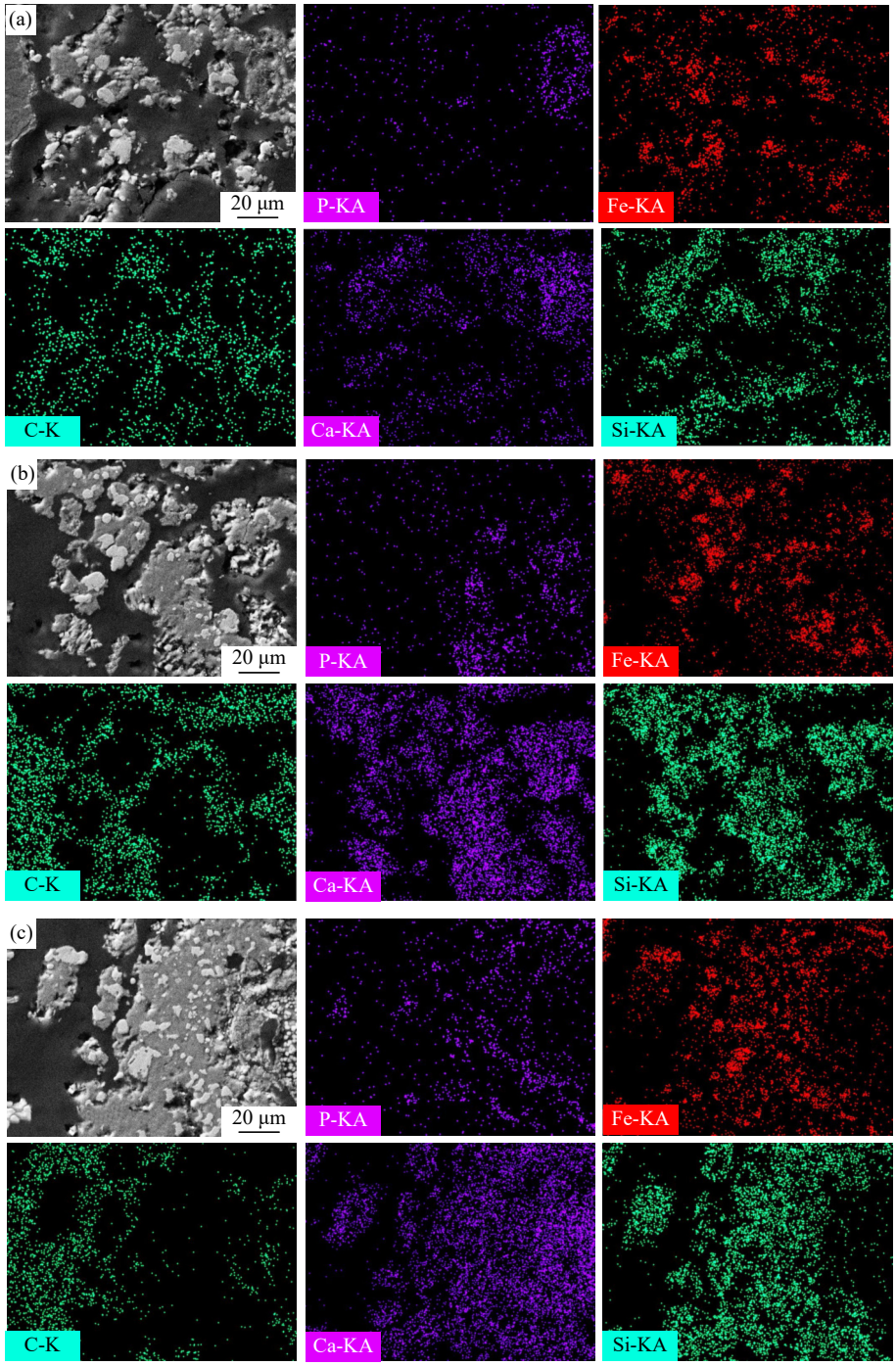


**Fig. 7. Representative SEM–EDS analyses of samples with different reduction times: (a) 20 min; (b) 40 min; (c) 60 min.**

phase, such as $NaAlSiO_4$, increased the amount of the liquid phase and promoted the kinetic conditions of mass transfer, favoring the occurrence of the dephosphorization reaction [34]. Moreover, alkali metals caused the lattice deformation of iron oxide to produce porous iron, which accelerated the diffusion of phosphorus gas [18].

The heat storage capacity of the sintering bed was enhanced in a hydrogen-rich atmosphere, and the extension of the high-temperature zone was beneficial to the occurrence of the apatite reduction reaction. The increase in the number of sintering zones with pores larger than 5 mm improved the air permeability of the sintering bed and was beneficial to the removal of phosphorus gas. However, the reduction temperature of iron oxide was lower than that of apatite, and a large amount of metallic iron was produced before apatite was reduced to $P_2$. Therefore, $P_2$ gas was partially absorbed by metallic iron to form iron–phosphorus compounds ($Fe_2P$), and the diffusion of phosphorus gas was the limiting link of its volatilization process. Moreover, because $Fe_3C$ and $Fe_2P$ were both hexagonal crystal systems and had similar lattice constants, the reduced $P_2$ was prone to migrate to the $Fe_3C$ lattice to form $Fe_2P$. The carburization reaction continuously increased the carbon content in the iron phase, further accelerating the migration of phosphorus to the iron phase, resulting in the decrease in the gasification dephosphorization rate [35].

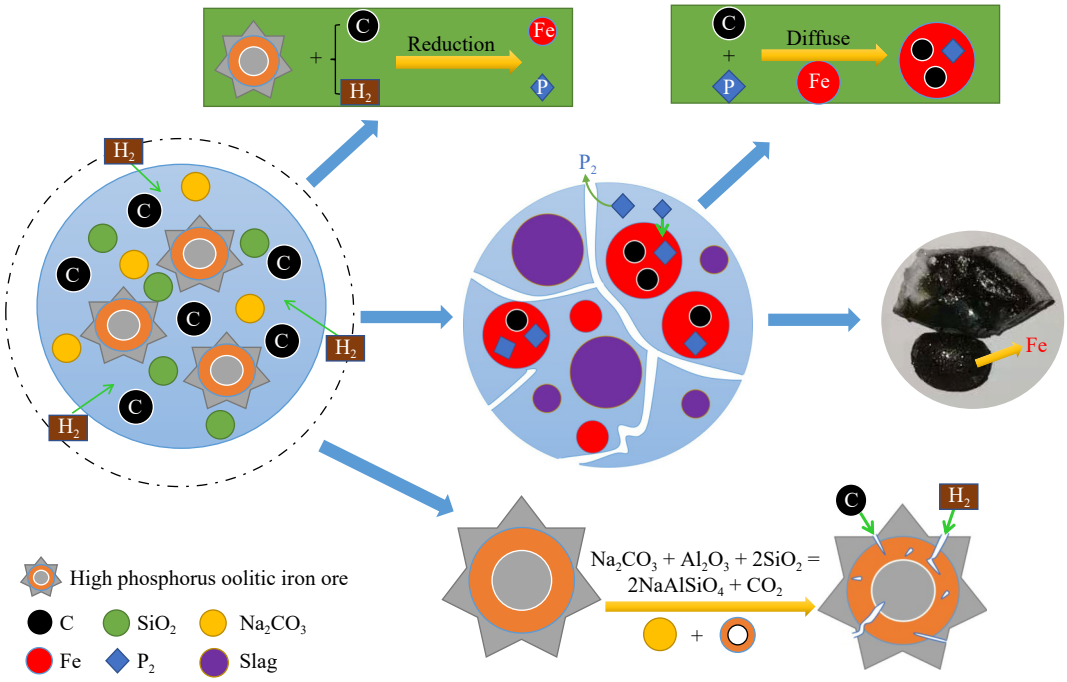


**Fig. 8. Schematic of the reduction mechanism in the hydrogen-rich sintering process of high-phosphorus iron ore.**

### 4.6. Practical application design of dephosphorization in the hydrogen-rich sintering reduction process

According to the traditional iron ore sintering principle, the entire sintering bed can be divided into the sintering zone, burning zone (700°C to the maximum temperature), preheating and drying zone (100 to 700°C), and over-wet zone (50 to 100°C) [36]. The schematic of the sintering bed distribution is shown in Fig. 9. Because of the effect of exhaust suction pressure, the sintering process proceeds from top to bottom. Under suction pressure, phosphorus gas produced by reduction during sintering moves downward along with flue gas. According to the previous experimental study, the dephosphorization rate first increased from 9.9% to 29.51% and then decreased to 8.62% at the temperature range of 900 to 1200°C, and the maximum value was obtained at 1100°C. The results of the dephosphorization rate at different reduction temperatures showed that the dephosphorization reaction mainly occurred in the sintering and burning zones.

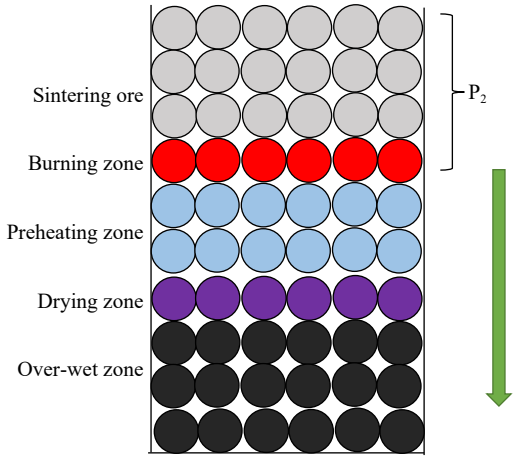


**Fig. 9. Schematic of sintering bed distribution.**

In the sintering and burning zones, the highest temperature is higher than 1300°C, and the sintering bed is subjected to a reducing atmosphere when injecting hydrogen-rich gas from the top, which can considerably reduce apatite. Then, the reduced phosphorus gas moves downward along with flue gas under suction pressure. In the preheating and drying zone, heat exchange occurs rapidly, and the waste gas temperature decreases from 1300 to 100°C. The boiling point of phosphorus is 280.5°C, and it will be condensed and adsorbed on the surface of the bed when passing through the low-temperature bed. Thus, phosphorus gas cannot be removed. In the over-wet zone, the waste gas from the upper bed contains a large amount of water vapor, which is cooled and recondensed when passing through the mixture, resulting in the over-wet phenomenon, which considerably reduces the permeability of the sintering bed and is inconducive to the discharge of phosphorus-containing gas.

In summary, the reduction and migration paths of phosphorus in the sintering bed involve the reduction and volatilization of apatite in the sintering and burning zones, and the reduced phosphorus gas moves downward along with flue gas under suction pressure. Part of the reduced phosphorus will be condensed and adsorbed on the surface of the bed when passing through the low-temperature bed, thus reducing the gasification dephosphorization rate. As the burning zone moves from the top to the bottom, phosphorus gas that condenses on the low-temperature bed will be re-reduced, re-volatilized, and recondensed until the sintering process completes and moves downward along with flue gas.

Fig. 10 shows the design diagram of the practical application of phosphorus gasification and recovery in the hydrogen-rich sintering process. The high-phosphate iron ore is first mixed with appropriate amounts of coke, flux, and additives and then evenly loaded into the trolley after mixing and pelletizing. During the sintering process, the mixture of hydro-

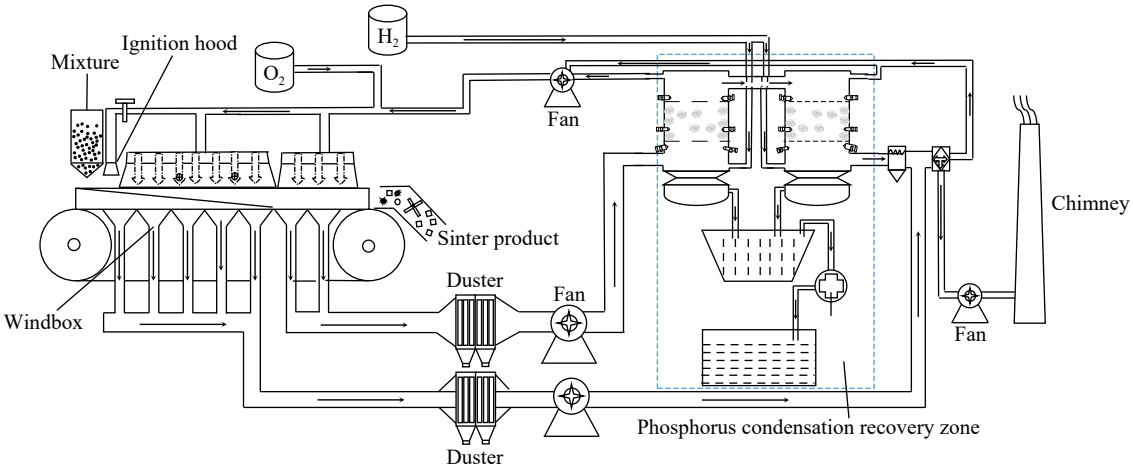


**Fig. 10. Schematic of phosphorus gasification and recovery in the hydrogen-rich sintering process of high-phosphorus iron ore.**

gen, oxygen, and circulating flue gas is injected into the sintering bed through a gas cover at a specific ratio. In the sintering process, apatite is reduced with the downward movement of the high-temperature bed, and the generated phosphorus gas is discharged with flue gas under the suction pressure of sintering. The dust impurities in the mixed flue gas are filtered by the duster, and phosphorus gas discharged with flue gas is collected by the condensation heat exchanger. Phosphorus gas is condensed into four-atom phosphorus molecules ($2P_2 \rightarrow P_4$) and gathered in the phosphorus collector, and the product, i.e., yellow phosphorus, is obtained after treatment. The mixed gas discharged from the condensing heat exchanger contains $H_2$, CO, and other reducing gases, which are recycled to the gas hood after purification and used as fuel.

## 5. Conclusions

(1) The experimental simulation proved that phosphorus removal by gasification in the hydrogen-rich sintering process was feasible, and the highest dephosphorization rate of 29.51% could be achieved. However, the selective reduction problem between iron oxide and apatite was encountered, and part of the reduced phosphorus gas was absorbed by iron, which limited the further increase in the dephosphorization rate.

(2) The reduction kinetics of apatite in the hydrogen-rich sintering process was investigated using the thermogravimetric technique and non-isothermal kinetic method. The activation energy of apatite reduction was 80.42 kJ/mol, and the most likely mechanism function was R2, a contracting cylinder. The differential form of the equation was $f(\alpha) = 2(1-\alpha)^{1/2}$, and the integral form of the equation was $G(\alpha) = 1-(1-\alpha)^{1/2}$.

(3) Apatite reduction was mainly concentrated in the sintering and burning zones, and phosphorus gas would be condensed and adsorbed on the surface of the bed when passing through the over-wet zone, thus considerably reducing the gasification removal rate.

(4) To improve the dephosphorization rate and prevent the condensation of phosphorus gas, auxiliary heating equipment can be added on both sides of the sintering machine. Moreover, the method for segmented recovery is adopted, and the negative pressure parameters are optimized to ensure a more efficient phosphorus collection and flue gas treatment.

## Acknowledgements

This work was financially supported by the National Natural Science Foundation of China (No. U1960205).

## Conflict of Interest

The authors have no relevant financial or non-financial interests to disclose.

## References

[1] Y. Jégourel, The global iron ore market: From cyclical developments to potential structural changes, *Extr. Ind. Soc.*, 7(2020), No. 3, p. 1128.

[2] X.Q. Hao, H.Z. An, X.Q. Sun, and W.Q. Zhong, The import competition relationship and intensity in the international iron ore trade: From network perspective, *Resour. Policy*, 57(2018), p. 45.

[3] J.X. Wu, J. Yang, L.W. Ma, Z. Li, and X.S. Shen, A system analysis of the development strategy of iron ore in China, *Resour. Policy*, 48(2016), p. 32.

[4] H. Baioumy, M. Omran, and T. Fabritius, Mineralogy, geochemistry and the origin of high-phosphorus oolitic iron ores of Aswan, Egypt, *Ore Geol. Rev.*, 80(2017), p. 185.

[5] J. Wu, Z.J. Wen, and M.J. Cen, Development of technologies for high phosphorus oolitic hematite utilization, *Steel Res. Int.*, 82(2011), No. 5, p. 494.

[6] S.C. Wu, Z.Y. Li, T.C. Sun, J. Kou, and X.H. Li, Effect of additives on iron recovery and dephosphorization by reduction roasting–magnetic separation of refractory high-phosphorus iron ore, *Int. J. Miner. Metall. Mater.*, 28(2021), No. 12, p. 1908.

[7] M. Altiner, Upgrading of iron ores using microwave assisted magnetic separation followed by dephosphorization leaching, *Can. Metall. Q.*, 58(2019), No. 4, p. 445.

[8] W.T. Zhou, Y.X. Han, Y.S. Sun, and Y.J. Li, Strengthening

iron enrichment and dephosphorization of high-phosphorus oolitic hematite using high-temperature pretreatment, *Int. J. Miner. Metall. Mater.*, 27(2020), No. 4, p. 443.

[9] Y.Y. Zhang, Q.G. Xue, H.B. Zuo, C. Cheng, G. Wang, F. Han, and J.S. Wang, Intermittent microscopic observation of structure change and mineral reactions of high phosphorus oolitic hematite in carbothermic reduction, *ISIJ Int.*, 57(2017), No. 7, p. 1149.

[10] E. Matinde and M. Hino, Dephosphorization treatment of high phosphorus iron ore by pre-reduction, air jet milling and screening methods, *ISIJ Int.*, 51(2011), No. 4, p. 544.

[11] L. Zhang, R. Machiela, P. Das, M.M. Zhang, and T. Eisele, Dephosphorization of unroasted oolitic ores through alkaline leaching at low temperature, *Hydrometallurgy*, 184(2019), p. 95.

[12] S.B. Kanungo and B.R. Sant, Dephosphorization of phosphorus-rich manganese ores by selective leaching with dilute hydrochloric acid, *Int. J. Miner. Process.*, 8(1981), No. 4, p. 359.

[13] M.J. Fisher-White, R.R. Lovel, and G.J. Sparrow, Phosphorus removal from goethitic iron ore with a low temperature heat treatment and a caustic leach, *ISIJ Int.*, 52(2012), No. 5, p. 797.

[14] C.N. Anyakwo and O.W. Obot, Phosphorus removal capability of aspergillus terreus and bacillus subtilis from Nigeria's agbaja iron ore, *J. Miner. Mater. Charact. Eng.*, 9(2010), No. 12, p. 1131.

[15] J. Tang, M.S. Chu, F. Li, C. Feng, Z.G. Liu, and Y.S. Zhou, Development and progress on hydrogen metallurgy, *Int. J. Miner. Metall. Mater.*, 27(2020), No. 6, p. 713.

[16] K. Gi, F. Sano, T. Homma, J. Oda, A. Hayashi, and K. Akimoto, An analysis on global energy-related $CO_2$ emission reduction and energy systems by current climate and energy policies and the nationally determined contributions, *J. Jpn. Inst. Energy*, 97(2018), No. 6, p. 135.

[17] V. Shatokha, E. Matukhno, K. Belokon, and G. Shmatkov, Potential means to reduce $CO_2$ emissions of iron and steel industry in Ukraine using best available technologies, *J. Sustain. Metall.*, 6(2020), No. 3, p. 451.

[18] D. Spreitzer and J. Schenk, Reduction of iron oxides with hydrogen—A review, *Steel Res. Int.*, 90(2019), No. 10, art. No. 1900108.

[19] N. Oyama, Y. Iwami, T. Yamamoto, S. Machida, T. Higuchi, H. Sato, M. Sato, K. Takeda, Y. Watanabe, M. Shimizu, and K. Nishioka, Development of secondary-fuel injection technology for energy reduction in the iron ore sintering process, *ISIJ Int.*, 51(2011), No. 6, p. 913.

[20] M.N. Abu Tahari, F. Salleh, T.S. Tengku Saharuddin, N. Dzakaria, A. Samsuri, M.W. Mohamed Hisham, and M.A. Yarmo, Influence of hydrogen and various carbon monoxide concentrations on reduction behavior of iron oxide at low temperature, *Int. J. Hydrogen Energy*, 44(2019), No. 37, p. 20751.

[21] M. Mizutani, T. Nishimura, T. Orimoto, K. Higuchi, S. Nomura, K. Saito, and E. Kasai, Influence of reducing gas composition on disintegration behavior of iron ore agglomerates, *ISIJ Int.*, 57(2017), No. 9, p. 1499.

[22] E.A. Mousa, A. Babich, and D. Senk, Enhancement of iron ore sinter reducibility through coke oven gas injection into the modern blast furnace, *ISIJ Int.*, 53(2013), No. 8, p. 1372.

[23] W. Gleason, An introduction to phosphorus: History, production, and application, *JOM*, 59(2007), No. 6, p. 17.

[24] M.A.M. Alzaky and D.X. Li, Sulfate of potash and yellow phosphorus to simultaneously remove $SO_2$–NO and obtain a complete fertilizer, *Atmos. Pollut. Res.*, 12(2021), No. 2, p. 147.

[25] W. Zhang, H.W Xing, T.L. Tian, and H. Wang, *Theory and Practice of Gasificating Dephosphorization in Sintering Process*, Metallurgical Industry Press, Beijing, 2016.

[26] Y.B. Chen and H.B. Zuo, Gasification behavior of phosphorus during pre-reduction sintering of medium-high phosphorus iron ore, *ISIJ Int.*, 61(2021), No. 5, p. 1459.

[27] S.K. El-Rahaiby and Y.K. Rao, The kinetics of reduction of iron oxides at moderate temperatures, *Metall. Trans. B*, 10(1979), No. 2, p. 257.

[28] H.S. Chen, Z. Zheng, Z.W. Chen, W.Z. Yu, and J.R. Yue, Multistep reduction kinetics of fine iron ore with carbon monoxide in a micro fluidized bed reaction analyzer, *Metall. Mater. Trans. B*, 48(2017), No. 2, p. 841.

[29] J.G. Santos, M.M. Conceição, M.F. Trindade, A.S. Araújo, V.J. Fernandes Jr, and A.G. Souza, Kinetic study of dipivaloylmethane by ozawa method, *J. Therm. Anal. Calorim.*, 75(2004), No. 2, p. 591.

[30] T. P. Bagchi and P.K. Sen, Kinetics of densification of powder compacts during the initial stage of sintering with constant rates of heating. A thermal analysis approach. Part I. Theoretical considerations, *Thermochim. Acta*, 56(1982), No. 3, p. 261.

[31] T. P. Bagchi and P.K. Sen, Kinetics of densification of powder compacts during the initial stage of sintering with constant rates of heating. A thermal analysis approach. Part III. Copper powder compacts, *Thermochim. Acta*, 61(1983), No. 1-2, p. 73.

[32] Q.H. Wu, J.Q. Li, X.D. Lv, B. Xv, C.Y. Chen, and R. Huang, Reaction mechanism of low-grade phosphate ore during vacuum carbothermal reduction, *Metall. Mater. Trans. B*, 52(2021), No. 3, p. 1484.

[33] P.M. Sargent and M.F. Ashby, Deformation mechanism maps for alkali metals, *Scripta Metall.*, 18(1984), No. 2, p. 145.

[34] Y.S. Sun, Y.F. Li, Y.X. Han, and Y.J. Li, Migration behaviors and kinetics of phosphorus during coal-based reduction of high-phosphorus oolitic iron ore, *Int. J. Miner. Metall. Mater.*, 26(2019), No. 8, p. 938.

[35] H. Sazegaran and S.M.M. Nezhad, Cell morphology, porosity, microstructure and mechanical properties of porous Fe–C–P alloys, *Int. J. Miner. Metall. Mater.*, 28(2021), No. 2, p. 257.

[36] D.Q. Zhu, S.W. Li, J. Pan, C.C. Yang, and B.J. Shi, Migration and distributions of zinc, lead and arsenic within sinter bed during updraft pre-reductive sintering of iron-bearing wastes, *Powder Technol.*, 342(2019), p. 864.